IEEE Access
Multidisciplinary | Rapid Review | Open Access Journal

Received September 27, 2021, accepted October 9, 2021, date of publication October 14, 2021, date of current version October 25, 2021.

Digital Object Identifier 10.1109/ACCESS.2021.3120273

Improved Linear Active Disturbance Rejection Control of Photovoltaic Grid Connected Inverter Based on Filter Function

BO ZHANG, XUESONG ZHOU, AND YOUJIE MA

Tianjin Key Laboratory for Control Theory & Applications in Complicated Industry Systems, School of Electrical and Electronic Engineering, Tianjin University of Technology, Tianjin 300384, China

Corresponding author: Bo Zhang (doctorzhang2022@163.com)

This work was supported in part by the National Natural Science Foundation of China under Grant 51877152, and in part by the Natural Science Foundation of Tianjin of China under Grant 18JCZDJC97300.

ABSTRACT Aiming at the problem of noise easily polluting the voltage measurement link of an inverter DC bus in photovoltaic grid, an improved linear active disturbance rejection control technology based on filter function is constructed by combining linear active disturbance rejection control technology with filter. The core of the method is to expand the filtered voltage into a new state variable and use the linear extended state observer to estimate the filtered voltage, which is used as the feedback quantity, to improve the ability of linear active disturbance rejection control technology to suppress high-frequency noise. Then, considering that the output of the system contains noise, the frequency domain characteristics of the improved linear active disturbance rejection control are analyzed theoretically and verified by Bode diagram simulation. Finally, the feasibility and effectiveness of the proposed control strategy are demonstrated by building a simulation platform for grid-connected PV inverter.

INDEX TERMS Photovoltaic grid connected system, linear active disturbance rejection control, linear extended state observer, frequency domain.

I. INTRODUCTION

An extensive amount of fossil fuel has caused severe damage to the environment, resulting in the deterioration of ecology. Therefore, it has studied all year round, and photovoltaic power generation has become the most important clean energy in the future. The grid-connected inverter acts as an adapter of renewable energy and grid, which plays a vital role in achieving high-efficiency power conversion and high-quality power supply [1]. The control of the inverter is not only responsible for adjusting the grid current but also for maintaining a stable voltage on the DC chain capacitor. If the DC voltage is not properly controlled, the system performance will decrease and even trigger the relevant protection device [2]. Therefore, the control performance of the DC-side voltage is an important indicator of reliability.

For photovoltaic grid inverters, a dual-ring control structure under a dq synchronous coordinate system is employed [3]. The external voltage ring maintains a constant DC link voltage through the power flow in the balance system, and the inner current loop handles power quality problems and harmonic protection. However, the system has disturbances, and the DC-side voltage fluctuates easily. These are mainly divided into three categories: (1) changed light, (2) changed temperature, and (3) fluctuating load.

The two-stage photovoltaic grid-connected system includes photovoltaic cell array, boost circuit DC/DC, inverter circuit DC/AC and other auxiliary devices [4]. Figure 1 shows the topology of the two-stage photovoltaic grid-connected power generation system. In the process of boosting, DC bus voltage oscillation is inevitable [5]–[7]. Excessive oscillation may cause the system to lose stability, and the inverter circuit can keep the bus voltage stable through reasonable control [8], [9].

PID controllers are commonly used in these systems, but they are not well adapted to parameter uncertainties, sudden change in climate conditions, and disturbances [10], [11].

Active disturbance rejection control (ADRC) is a new control algorithm that has been proposed in recent years. It considers the unmodeled part and unknown disturbance in

The associate editor coordinating the review of this manuscript and approving it for publication was Mira Naftaly.

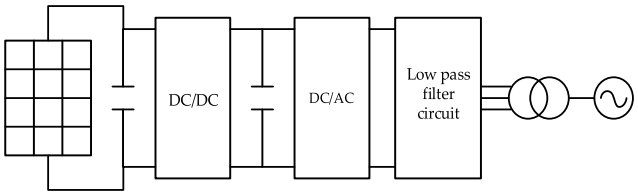

FIGURE 1. Operation model diagram of photovoltaic power generation.

the controlled object as a system disturbance, estimates them using an extended state observer (ESO), and compensates them in dynamic feedback. It can compensate the nonlinear, multi-variable, uncertain and uncertain disturbances, and strong coupling systems have good control effect [12], [13]. However, in the original ADRC, ESO and error feedback control rate are presented as nonlinear functions, and there are many tuning parameters, which is not convenient for practical applications. To solve this problem, Professor Gao Z.Q. proposed linear active disturbance rejection control (LADRC) based on linear processing of the above two links, and determined the controller parameters by using bandwidth, which made the whole system easy to debug and practical applications [14]. Although LADRC has strong disturbance rejection and tracking performance, the large gain coefficient of LESO will also cause noise amplification problems, which will affect the stability of the controller [15]. To solve the noise sensitivity of LESO, scholars at home and abroad have proposed many different solutions. The method of switching LESO gain was used in reference [16]. The research shows that the improved LADRC can quickly estimate the system state and effectively suppress the measurement noise at the output. In [17], an adaptive variable gain observer was proposed to suppress the influence of noise on the system without changing the original characteristics of LESO. Although the above scheme can better suppress the impact of noise on the system output, the design is more complex, and engineering applications are difficult. In [18], a predictive tracking differential active disturbance rejection controller was proposed, which can suppress the influence of noise and reduce the phase delay; however, it has the problems of poor dynamic performance and difficult parameter tuning. In [19], the filter equation was extended to ESO, and the influence of output noise on the system was solved well. However, nonlinear ADRC was used in this study, and parameter tuning was difficult.

The three-phase components and loads are often not matched, resulting in a three-phase voltage and current imbalance at the power supply point. In addition, a faulty system may also lead to three-phase unbalance. A three-phase unbalanced will increase the line loss. The control measures of three-phase unbalanced are mainly by adjusting the reactive power. ADRC can adjust the three-phase unbalance by controlling the rectifier. In order to analyze the needs, this paper mainly focuses on the symmetrical system [20].

In this study, the filter equation is combined with the second-order LADRC to construct an improved LADRC

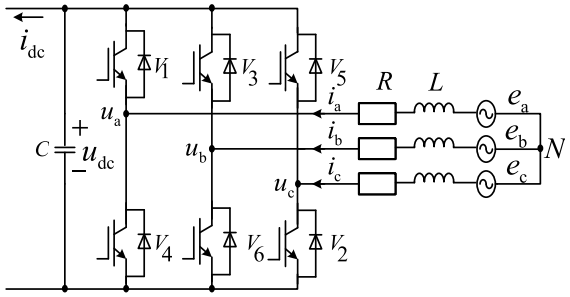

FIGURE 2. Structure diagram of inverter system.

based on the filter function, and the anti-interference, noise suppression and stability of the improved LADRC were analyzed. Under the premise of ensuring system stability, the noise can be effectively suppressed. Finally, the feasibility of the control strategy is verified by building a simulation platform.

II. MATHEMATICAL MODEL OF THE GRID-SIDE CONVERTER

In general, because the output voltage of photovoltaic cells is usually lower than the voltage working range of inverter, the DC output from photovoltaic cells should pass through the DC/DC boost converter before the energy is delivered to the DC/AC converter [21]. The DC/AC converter adopts a three-phase full-bridge inverter circuit. A typical topology is presented in [22].

Assuming that the current reference direction is the direction of the grid flowing into the inverter, according to Kirchhoff laws, the mathematical model in three-phase static coordinate system can be obtained as

$$\begin{cases} L\dfrac{di_a}{dt} = e_a - Ri_a - u_a \\ L\dfrac{di_b}{dt} = e_b - Ri_b - u_b \\ L\dfrac{di_c}{dt} = e_c - Ri_c - u_c \\ C\dfrac{dU_{dc}}{dt} = S_a i_a + S_b i_b + S_c i_c - i_{dc} \end{cases} \tag{1}$$

In formula (1), e_a, e_b, and e_c are grid voltages; i_a, i_b, and i_c are grid currents; u_a, u_b, and u_c are output voltages of the three-phase grid-side inverter, L is the equivalent filter inductance, R is equivalent resistance, U_{dc} is the DC bus capacitor voltage, i_{dc} is the DC side output current, S_a, S_b, and S_c are the switching functions of each phase bridge arm respectively. If S_a is the pulse of 0/1 corresponding to the open/close of the coupling lower bridge arms, for which S_a can be modeled as function (2):

$$S_a = \begin{cases} 1 & S_1 \text{ close, } S_4 \text{ open} \\ 0 & S_1 \text{ open, } S_4 \text{ close} \end{cases}$$

$$S_b = \begin{cases} 1 & S_3 \text{ close, } S_6 \text{ open} \\ 0 & S_3 \text{ open, } S_6 \text{ close} \end{cases}$$

$$S_c = \begin{cases} 1 & S_5 \text{ close, } S_2 \text{ open} \\ 0 & S_5 \text{ open, } S_2 \text{ close} \end{cases} \tag{2}$$

Because the three phases are coupled with each other, which is not conducive to the design of the control system, the mathematical model of the grid-connected inverter in the dq coordinate system is obtained by using the coordinate transformation method.

$$\begin{cases} L\dfrac{di_{\mathrm{d}}}{dt} = e_{\mathrm{d}} - u_{\mathrm{d}} - Ri_{\mathrm{d}} + \omega_g Li_{\mathrm{q}} \\ L\dfrac{di_{\mathrm{q}}}{dt} = e_{\mathrm{q}} - u_{\mathrm{q}} - Ri_{\mathrm{q}} - \omega_g Li_{\mathrm{d}} \\ C\dfrac{dU_{\mathrm{dc}}}{dt} = \dfrac{3}{2}\sum\limits_{k=\mathrm{d,q}} S_k i_k - i_{\mathrm{dc}} \end{cases} \tag{3}$$

In equation (3), e_{d} and e_{q} are the components of the grid voltage on the dq axis of the rotating coordinate system, respectively; i_{d} and i_{q} are the components of the grid-side current on dq axis of rotating coordinate system, u_{d} and u_{q} are the components of the grid-side inverter output phase voltage on the dq axis of the rotating coordinate system, and the component of the switching function on the dq axis of rotating coordinate system is $\mathrm{S_k}$, ω_g is the grid frequency, $k = a, b, c$.

Although the physical meaning of the mathematical model of the grid-side converter in a three-phase static coordinate system is clear, the design of the control system becomes complicated because of the coupled sinusoidal time-varying parameters in the model. Therefore, after the Park transformation, the mathematical model shown in equation (1) is transformed into a mathematical model in the dq coordinate system, which rotates synchronously with the fundamental voltage of the power grid to realize decoupling control.

Through the above mathematical transformation, we can better use mathematical means to control the inverter, to ensure the normal operation of the system.

If the photovoltaic system is to be grid connected, the grid-connected inverter must reverse the DC power into AC power with the same voltage, phase and frequency as the grid. With the existence of all kinds of working conditions, the grid-connected system also needs to have a certain anti-interference ability, such as environment mutation, load mutation, etc. The inverter control can stabilize the DC bus voltage, and the implementation method is voltage outer loop control, the output power also needs certain control, and the implementation means is the current inner loop control [23]–[25]. At the same time, the outer voltage loop and the inner current loop control can meet the requirements of grid-connected disturbance rejection, this study uses a double closed-loop control strategy. The input of the current inner loop is the feedback value of the grid voltage. In this study, the active and reactive power are controlled separately.

The grid voltage vector E rotates synchronously with the dq axis of the rotation coordinate, so that the d axis overlaps with the grid voltage vector E. figure 3 shows the vector diagram of the system output.

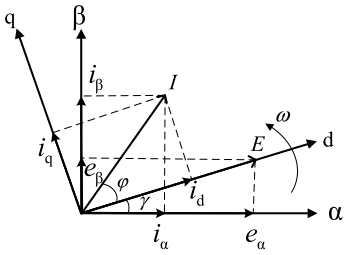

FIGURE 3. System output vector diagram.

The projection of grid voltage on dq axis can be got from figure 3.

$$\begin{cases} e_{\mathrm{d}} = |E| \\ e_{\mathrm{q}} = 0 \end{cases} \tag{4}$$

According to figure 3, the instantaneous output power of the grid-connected inverter can be obtained as

$$\begin{cases} P = \dfrac{3}{2}(i_{\mathrm{d}}e_{\mathrm{d}} + i_{\mathrm{q}}e_{\mathrm{q}}) \\ Q = \dfrac{3}{2}(i_{\mathrm{d}}e_{\mathrm{q}} - i_{\mathrm{q}}e_{\mathrm{d}}) \end{cases} \tag{5}$$

From the above, it can be concluded that:

$$\begin{cases} P = \dfrac{3}{2}i_{\mathrm{d}}e_{\mathrm{d}} \\ Q = -\dfrac{3}{2}i_{\mathrm{q}}e_{\mathrm{d}} \end{cases} \tag{6}$$

If the fluctuation of the grid voltage is ignored, the component e_{d} of grid voltage on the d-axis can be regarded as a constant. From equation (6), it can be seen that the instantaneous output power of the grid-connected inverter is only related to the component of current vector on the dq axis. The control i_{d} can control P, and the control i_{q} can control Q. If the losses of filter and inverter at AC side are ignored, the expression of active power at DC side of inverter is as follows:

$$P = u_{\mathrm{dc}}i_{\mathrm{dc}} = \frac{3}{2}e_{\mathrm{d}}i_{\mathrm{d}} \tag{7}$$

According to the above derivation, an overall control structure block diagram of the grid-connected inverter can be constructed.

As shown in figure 4, the inverter control structure adopts double closed-loop control, the outer loop uses a voltage loop, and the inner loop is a current loop. The input of the structure diagram is the given value u^*_{dc} of the DC bus voltage. The actual DC bus voltage value was measured, and the error is calculated and adjusted by ADRC to obtain the given value i^*_{d} of d-axis current [26]. To improve the power factor, it is better to make the reactive power 0, and then set the given value $i^*_{\mathrm{q}} = 0$ such that the inverter can only transmit active power. Finally, i^*_{d} and i^*_{q} of the inner current loop are compared with the actual value respectively, and are sent to the Space Vector Pulse Width Modulation (SVPWM) module through the PI regulator and Clark transform to drive the switching elements of the inverter.

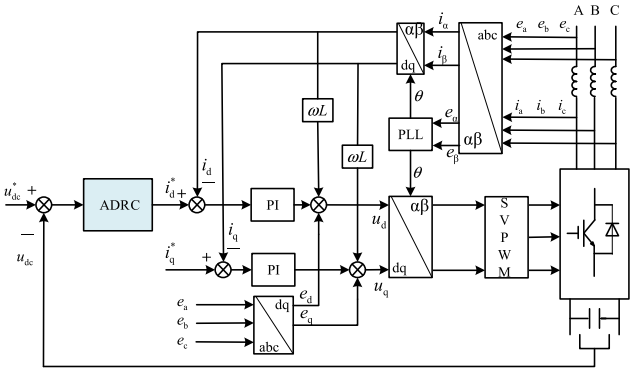

FIGURE 4. Overall control structure block diagram of grid connected inverter.

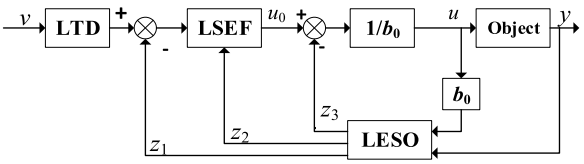

FIGURE 5. Structure diagram of traditional LADRC.

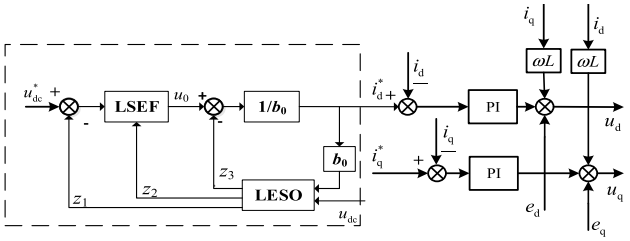

FIGURE 6. Grid connected inverter structure of LADRC voltage outer loop.

III. DESIGN OF THE LADRC CONTROLLER

A. ANALYSIS OF TRADITIONAL LADRC CONTROL PRINCIPLE

The LADRC is composed of linear tracking differentiator (LTD), linear extended state observer (LESO) and linear state error feedback (LSEF), as shown in figure 5. The function of LTD is to extract the differential signal and track the input signal quickly without overshoot [27]. To avoid the high-frequency oscillation of the capacitor voltage caused by using the tracking differentiator, the tracking differentiator is not used.

In figure 5, y is the system output, u is the controller output z_1, z_2, and z_3 are the observer's observation value of each state variable and the total disturbance of the system, v is the reference input, and b_0 is the controller gain.

The system structure is shown in figure 6.

Because the switching period (10 $\sim$ 30kHz) of the switch tube is much higher than the power frequency period (50 Hz) of the power grid, the switching function S_k can be linearized according to reference [28].

Because the mathematical model of grid-connected inverter is a second-order system, a second-order LADRC controller was designed [29]. The control strategy is controlled by the voltage directional vector, and the Q-axis current is set to zero, so the formula can be changed to:

$$\frac{d^2U_{dc}}{dt^2} = \frac{3}{2LC}\sum_{k=d,q} S_k\left(e_k - u_k - i_k R\right) - \frac{\omega}{2C}\left(S_q i_d - S_d i_q\right) \tag{8}$$

According to formula (8), the following form of the state-space equation can be obtained

$$\begin{cases} \begin{bmatrix} \dot{x}_1 \\ \dot{x}_2 \\ \dot{x}_3 \end{bmatrix} = \begin{bmatrix} 0 & 1 & 0 \\ 0 & 0 & 1 \\ 0 & 0 & 0 \end{bmatrix} \begin{bmatrix} x_1 \\ x_2 \\ x_3 \end{bmatrix} + \begin{bmatrix} 0 & 0 \\ 0 & b_0 \\ 1 & 0 \end{bmatrix} \begin{bmatrix} h \\ u \end{bmatrix} \\ y = x_1 \end{cases} \tag{9}$$

where x_1 and x_2 are the DC bus voltage and its differential respectively, and x_3 is a newly expanded state variable, representing the total disturbance of the system, denoted as f. The voltage outer loop LADRC records the parameter uncertainties, time variables, external disturbances, grid-side voltage components about the d and q axes, and load output current in the system mathematical model as the total disturbance f of the grid-connected inverter. LADRC first uses LESO to observe f, and then uses the disturbance compensation link to eliminate the influence of f on the system. Therefore, the control strategy can effectively suppress the disturbance caused by a change in the power grid voltage. Where h is the differential of the total disturbance and $b_0 = 3/(2LC)$ [30]. According to Eq (8), the total disturbance can be recorded as:

$$f = \frac{3}{2LC}\sum_{k=d,q} S_k\left(-i_k R - u_k\right) - \frac{\omega}{2C}\left(S_q i_d - S_d i_q\right) + \frac{3S_q u_q}{2LC} \tag{10}$$

According to equation (9), a third-order LESO can be constructed:

$$\begin{cases} \dot{z}_1 = z_2 - \beta_1\left(z_1 - y\right) \\ \dot{z}_2 = z_3 - \beta_2\left(z_1 - y\right) + b_0 u \\ \dot{z}_3 = -\beta_3\left(z_1 - y\right) \end{cases} \tag{11}$$

where z_1, z_2, and z_3 are the observed values of the DC bus voltage, DC bus voltage differential and total disturbance respectively, β_1, β_2, and β_3 are the observer gain. Choose the right of β_1, β_2, and β_3. LESO will realize the real-time tracking of each state variable in formula (9), namely $z_1 \rightarrow x_1, z_2 \rightarrow x_2, z_3 \rightarrow x_3$.

LESF is designed as follows:

$$u_0 = k_p\left(v - z_1\right) - k_d z_2 \tag{12}$$

where, k_p and k_d are the controller parameters. Taking the disturbance compensation link as:

$$u = \frac{u_0 - z_3}{b_0} \tag{13}$$

If the error between z_3 and f is ignored, Equation (9) can be simplified as an integral series structure. According to the

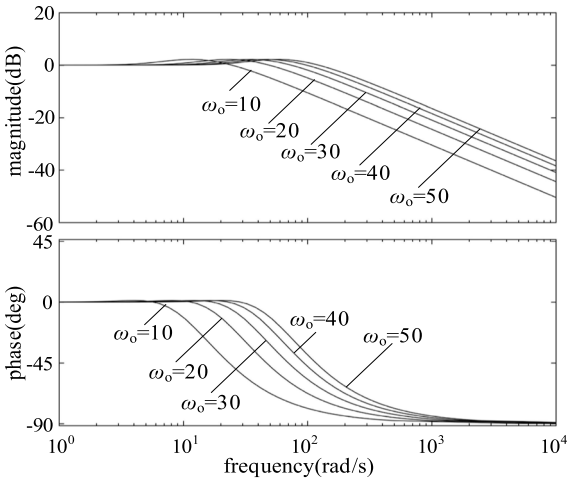

FIGURE 7. Frequency domain characteristic curve of observation noise.

pole assignment method, the following pole assignment can be performed:

$$\begin{cases} \beta_1 = 3\omega_o \\ \beta_2 = 3\omega_o^2 \\ \beta_3 = \omega_o^3 \end{cases} \tag{14}$$

$$\begin{cases} k_p = \omega_c^2 \\ k_d = 2\omega_c \end{cases} \tag{15}$$

where, ω_o and ω_c are the bandwidths of the observer and the controller respectively. Through the above pole assignment, LADRC only needs to adjust three parameters b_0, ω_o and ω_c.

B. STRUCTURE DESIGN OF IMPROVED LADRC

According to the (11) and (14), we can obtain the transfer functions of z_1, z_2 and z_3.

$$\begin{cases} z_1 = \dfrac{3\omega_o s^2 + 3\omega_o^2 s + \omega_o^3}{(s+\omega_o)^3} y + \dfrac{b_0 s}{(s+\omega_o)^3} u \\ z_2 = \dfrac{\left(3\omega_o^2 s + \omega_o^3\right) s}{(s+\omega_o)^3} y + \dfrac{b_0 (s+3\omega_o) s}{(s+\omega_o)^3} u \\ z_3 = \dfrac{\omega_o^3 s^2}{(s+\omega_o)^3} y - \dfrac{b_0 \omega_o^3}{(s+\omega_o)^3} u \end{cases} \tag{16}$$

The reference [31] proved that the traditional LESO has good anti-interference performance and convergence. If we consider the influence of the noise δ of the output y on the third-order LESO. The transfer function of noise can be obtained from (16)

$$\frac{z_1}{\delta} = \frac{3\omega_o s^2 + 3\omega_o^2 s + \omega_o^3}{(s+\omega_o)^3} \tag{17}$$

The frequency domain characteristic curve of figure 7 can be obtained when $\omega = 10$, 20, 30, 40, and 50:

It can be seen from figure 7 that with the increase in ω_o, the gain of high-frequency band increases significantly, and the amplification effect on noise becomes more obvious.

Although LESO has a strong anti-interference ability, it is sensitive to noise because of the large gain of the controller. There is a lot of noise pollution in practical engineering; if not treated, it will cause system output chattering and reduce the life of the actuator; in severe cases, the stability of the controller will be reduced. Therefore, the system output must be considered to be polluted by noise.

C. IMPROVED LADRC DESIGN

It is assumed that the output of the controlled object contains the measurement noise δ, that is $y = x_1 + \delta$. To reduce the output noise, the filtered bus voltage signal is used as the feedback input of the controller, and the filtered state variable is defined as x_0.

$$x_0(s) = \frac{1}{Ts+1} y = \frac{\omega}{s+\omega} y \tag{18}$$

In equation (18), T is the time constant, and ω is the cut-off frequency of the first-order low-pass filter, $\omega = 1/T$.

The equation of state of the system can be obtained by simultaneous formulas (9) and (18).

$$\begin{cases} \dot{x}_0 = -\omega x_0 + \omega y \\ \dot{x}_1 = x_2 \\ \dot{x}_2 = x_3 + b_0 u \\ \dot{x}_3 = h \\ y_0 = x_0 \end{cases} \tag{19}$$

In equation (19), y_0 is the output of the system after filtering. At this time, the output does not contain high-frequency noise, which eliminates the influence of noise on the controller. The fourth-order LESO can be constructed using Equation (19).

$$\begin{cases} \dot{z}_0 = -\omega z_0 + \omega z_1 - \beta_0 e_0 \\ \dot{z}_1 = z_2 - \beta_1 e_0 \\ \dot{z}_2 = z_3 - \beta_2 e_0 + b_0 u \\ \dot{z}_3 = -\beta_3 e_0 \end{cases} \tag{20}$$

In equation (20), β_0, β_1, β_2, and β_3 is the observer gain and z_0 are the observed value of x_0. $e_0 = z_0 - y_0$ is defined as the observation error of LESO pair. Noise suppression and disturbance compensation can be realized by choosing an appropriate observer gain.

According to the pole placement method, the characteristic equation of (20) is an ideal form to realize fast and no overshoot tracking of the reference signal

$$\begin{cases} \beta_0 = 4\omega_o - \omega \\ \beta_1 = 6\omega_o^2/\omega \\ \beta_2 = 4\omega_o^3/\omega \\ \beta_3 = \omega_o^4/\omega \end{cases} \tag{21}$$

Therefore, the control structure block diagram of the improved LADRC can be obtained, as shown in figure 8.

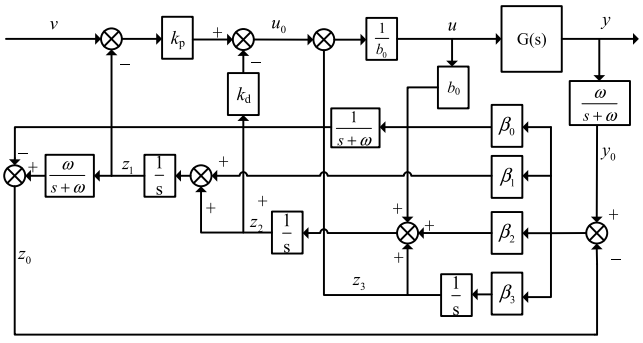

FIGURE 8. Structure diagram of improved LADRC.

The transfer functions of the improved LESO observations can be calculated using equation (20) and (21).

$$\begin{cases} z_0 = \dfrac{(4\omega_o - \omega)\, s^3 + 6\omega_o s^2 + 4\omega_o^3 s + \omega_o^4}{(s+\omega_o)^4} y_0 \\ \quad + \dfrac{\omega s}{(s+\omega_o)^4} b_0 u \\ z_1 = \dfrac{\beta_0 s^3 + (\beta_1 + \beta_0\omega)\, s^2 + (\beta_2 + \beta_1\omega)\, s + \omega\beta_2}{(s+\omega_o)^4} y_0 \\ \quad + \dfrac{s^2 + 4\omega_o s}{(s+\omega_o)^4} b_0 u \\ z_2 = \dfrac{\beta_1 s^3 + (\beta_2 + \beta_1\omega)\, s^2 + \omega\beta_2 s}{(s+\omega_o)^4} y_0 \\ \quad + \dfrac{s^3 + 4\omega_o s^2 + 6\omega_o^2 s}{(s+\omega_o)^4} b_0 u \\ z_3 = \dfrac{\beta_2 s^3 + \omega\beta_2 s^2}{(s+\omega_o)^4} y_0 - \dfrac{\omega_o^4}{(s+\omega_o)^4} b_0 u \end{cases} \tag{22}$$

Let the tracking error $e_1 = z_1 - x_1, e_2 = z_2 - x_2$, the following results can be obtained:

$$\begin{cases} e_0 = -\dfrac{s^3\,(s+\omega)}{(s+\omega_o)^4} y_0 + \dfrac{\omega s}{(s+\omega_o)^4} b_0 u \\ e_1 = -\dfrac{s^3\,(s+\omega)\,(s+4\omega_o)}{\omega\,(s+\omega_o)^4} y_0 + \dfrac{s\,(s+4\omega_o)}{(s+\omega_o)^4} b_0 u + \delta(s) \\ e_2 = -\dfrac{s^3\,(s+\omega)\left(s^2 + 4\omega_o s + 6\omega_o^2\right)}{\omega\,(s+\omega_o)^4} y_0 \\ \quad + \dfrac{s\left(s^2 + 4\omega_o s + 6\omega_o^2\right)}{(s+\omega_o)^4} b_0 u + s\delta(s) \end{cases} \tag{23}$$

Let $e_3 = z_3 - f$. Then according to equation (19), we can obtain $f = x_3 = \ddot{x}_1 - b_0 u$, from which we can further calculate:

$$e_3 = -\left(1 - \frac{\omega_o^4}{(s+\omega_o)^4}\right) \frac{s^2(s+\omega)}{\omega} y_0 + \left(1 - \frac{\omega_o^4}{(s+\omega_o)^4}\right) \times b_0 u + s^2\delta(s) \tag{24}$$

Considering the typicality of the analysis, y_0 and u all take the step signal with an amplitude of K, $y_0(s) = K/s$, $u(s) = K/s$, and the steady-state error can be obtained:

$$\begin{cases} e_{0s} = \lim\limits_{s\to 0} s e_0 = 0 \\ e_{1s} = \lim\limits_{s\to 0} s e_1 = 0 \\ e_{2s} = \lim\limits_{s\to 0} s e_2 = 0 \\ e_{3s} = \lim\limits_{s\to 0} s e_3 = 0 \end{cases} \tag{25}$$

Equation (25) indicates that improved LESO has good convergence capability and tracking capabilities, enabling system state variables and non-deviation estimates for disturbances.

From formulas (12), (13), and (15), it can be concluded that:

$$u_o = \frac{1}{b_0}\left(\omega_c\,(v - z_1) - 2\omega_c z_2 - z_3\right) \tag{26}$$

By substituting formula (22), it can be calculated that:

$$u = \frac{1}{b_0} \frac{A_1}{A_1 + A_2 s^3 + A_3 s^2 + A_4 s - A_5} (A_6 v - \frac{(s+\omega)\left(A_7 s^2 + A_8 s + A_9\right)}{\omega A_1} y_0) \tag{27}$$

where:

$$\begin{cases} A_1 = (s+\omega_o)^4 \\ A_2 = 2\omega_c \\ A_3 = \omega_c^2 + 8\omega_o\omega_c \\ A_4 = 12\omega_o^2\omega_c + 4\omega_o\omega_c^2 \\ A_5 = \omega_o^4 \\ A_6 = \omega_c^2 \\ A_7 = \omega_o^4 + 8\omega_o^3\omega_c + 6\omega_o^2\omega_c^2 \\ A_8 = 12\omega_o^4\omega_c + 4\omega_o^3\omega_c^2 \\ A_9 = \omega_o^4\omega_c^2 \end{cases}$$

According to equation (26), the simplified structure diagram of the system can be obtained as follows:

In figure 9:

$$G_1(s) = \frac{A_1}{A_1 + A_2 s^3 + A_3 s^2 + A_4 s - A_5}$$
$$H(s) = \frac{A_7 s^2 + A_8 s + A_9}{A_1}$$
$$G_e(s) = \frac{s+\omega}{\omega}$$

Combined with formula (19), the controlled object can be recorded as:

$$y_0 = \frac{\omega}{(s+\omega)s^2}(f + b_0 u) + \frac{\omega}{(s+\omega)}\delta \tag{28}$$

According to figure 9, the closed-loop transfer function of the system output is as follows:

$$y_0 = \frac{\omega\omega_c^2}{(s+\omega)(s+\omega_c)^2} v + \frac{\omega\left(s^6 + C_1 s^5 + C_2 s^4 + C_3 s^3\right)}{(s+\omega_o)^4 (s+\omega_c)^2 (s+\omega)}\delta + \frac{\omega\left(s^4 + C_1 s^3 + C_2 s^2 + C_3 s\right)}{(s+\omega_o)^4 (s+\omega_c)^2 (s+\omega)} f \tag{29}$$

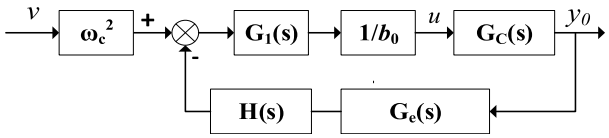

FIGURE 9. Simplified system structure diagram.

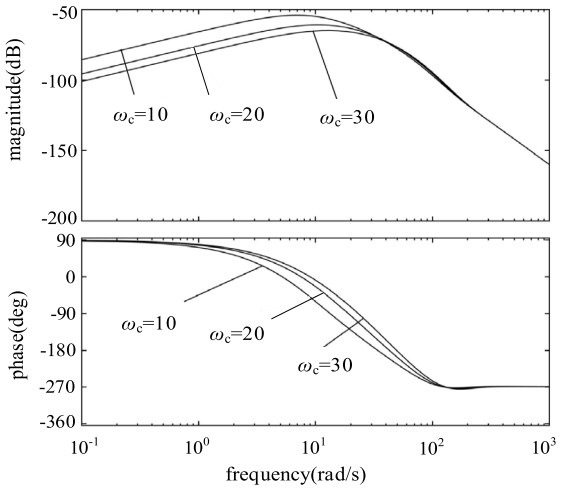

FIGURE 10. Frequency domain characteristic curve of disturbance term (ω_c change).

where:

$$\begin{cases} C_1 = 4\omega_o + 2\omega_c \\ C_2 = 6\omega_o^2 + 8\omega_o\omega_c + \omega_c^2 \\ C_3 = 4\omega_o^3 + 12\omega_o^2\omega_c + 4\omega_o\omega_c^2 \end{cases}$$

According to the formula (29), the system output consists of a trace item, an interference item, and a noise item. When ignoring interference and noise items, the system output contains only tracking items. Taking the cut-off frequency of the first-order low-pass filter ω in this case, the control performance of the system depends only on the bandwidth of the controller ω_c. The larger the bandwidth of the controller, the faster the tracking speed, and the disturbance term of system output and its relation ω, ω_o, ω_c, the cut-off frequency of the filter is fixed at $\omega = 10$. Observe the frequency characteristics of the system when ω_o and ω_c change.

It can be observed from the figure 10 and 11 that with an increasing in ω_o and ω_c, the low-frequency gain of the system decreases, the bandwidth increases obviously, and the high-frequency gain of the system remains unchanged; thus, the anti-interference ability of the system increases. It can be seen from the figure that with the increase in ω_c and ω_o, the phase lag of the system decreases, and the observation and tracking ability of disturbance increases.

When ω_c and ω_o remain unchanged and the cut-off frequency ω of the filter changes, the frequency-domain characteristic curve of the system is shown in figure 12.

As can be seen from figure 12, as ω increases, the low frequency gain of the system remains unchanged, that is, the change in the cutoff frequency of the filter is not affected

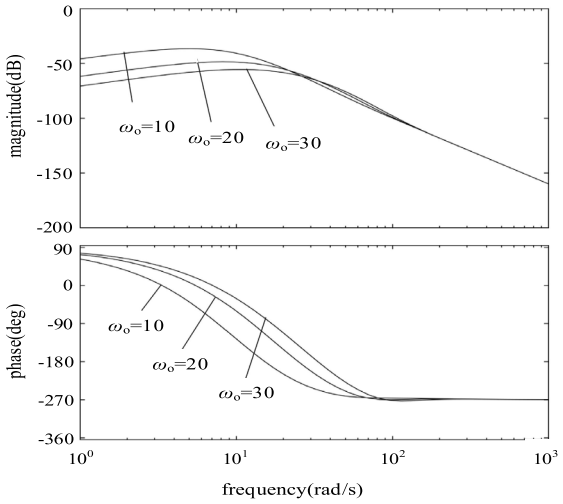

FIGURE 11. Frequency domain characteristic curve of disturbance term (ω_o change).

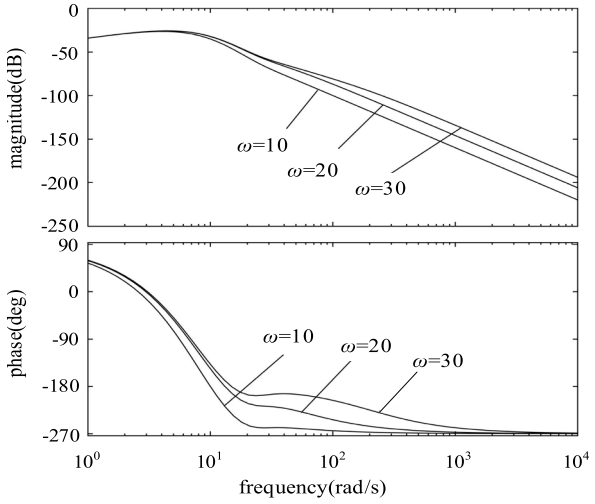

FIGURE 12. Frequency domain characteristic curve of disturbance term (ω change).

by the anti-interference performance of the low frequency band; at the same time, the high frequency gain of the system increases, the system high frequency anti-interference ability is reduced. Therefore, ω should not be excessively large.

It can be seen from equation (29) that the noise term of the system output is related to ω, ω_o, ω_c. The cut-off frequency of the filter is $\omega = 10$, and the frequency characteristics of the system are observed when ω_o and ω_c change.

As shown in figures 13 and 14 with an increase in ω_o and ω_c, the noise suppression ability of the system is enhanced, the phase lag of the system is reduced, and the observation and tracking ability of noise is enhanced.

When the values of ω_o and ω_c remain unchanged and the cut-off frequency ω of the filter changes, the frequency-domain characteristic curve of the system is shown in figure 15.

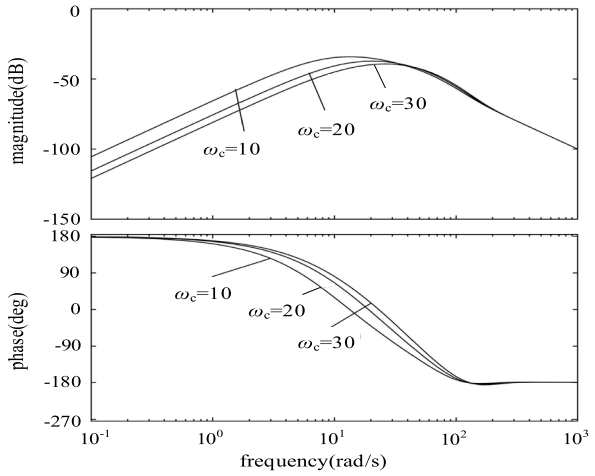

FIGURE 13. Frequency domain characteristic curve of noise term (ω_c change).

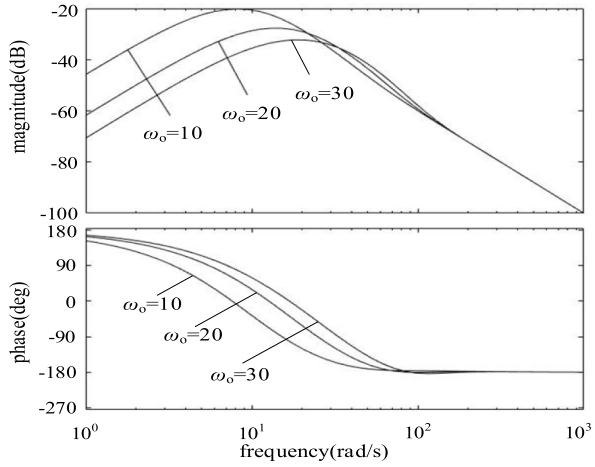

FIGURE 14. Frequency domain characteristic curve of noise (ω_o change).

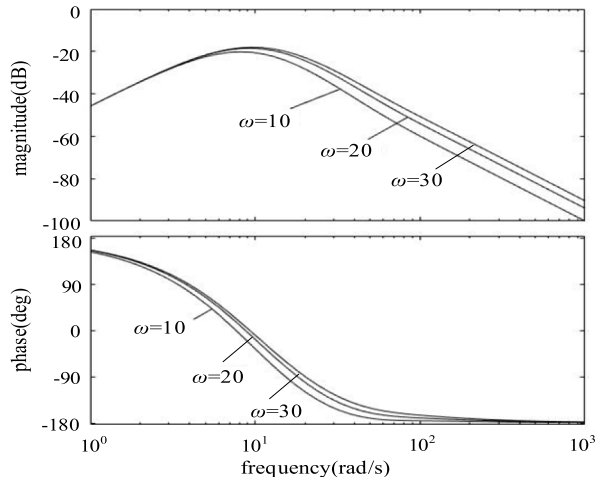

FIGURE 15. Frequency domain characteristic curve of noise term (ω change).

It can be seen from figure 15 that the ability of the system to suppress high-frequency noise is weakened owing to excessive ω, which is similar to the characteristics of the first-order low-pass filter. The larger the ω, the larger the allowed frequency, and the weaker the noise-suppression ability.

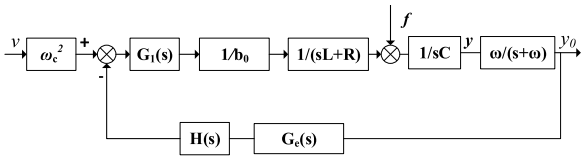

FIGURE 16. System structure of improved LADRC photovoltaic inverter.

According to figure 9, the actual structure of the grid-connected photovoltaic inverter can be constructed, as shown in the figure below.

According to figure 16, the closed-loop transfer function of the actual system can be obtained as follows:

$$y_0 = \frac{\omega\omega_c G_1(s)}{(s+\omega)(b_0(LCs^2+RCs)+G_1(s)H(s))}v \tag{30}$$

From equations (26) and (30), it can be concluded that:

$$y_0 = \frac{\omega\omega_c(s+\omega_o)^4}{a_7s^7+a_6s^6+a_5s^5+a_4s^4+a_3s^3+a_2s^2+a_1s+a_0}v \tag{31}$$

In equation (31):

$$\begin{cases} a_7 = b_0CL \\ a_6 = b_0C(R+4L\omega_o+2L\omega_c+L\omega) \\ a_5 = RCb_0(4\omega_o+2\omega_c+\omega)+LCb_0 \\ \quad \times(6\omega_o^2+\omega_c^2+8\omega_o\omega_c+4\omega_o\omega+2\omega_c\omega) \\ a_4 = LCb_0\left(4\omega_o^3+4\omega_o\omega_c^2+12\omega_o^2\omega_c\right) \\ \quad + LCb_0\left(6\omega_o^2\omega+\omega_c^2\omega+\omega_o\omega_c\omega\right) \\ \quad + RCb_0\left(6\omega_o^2+\omega_c^2+8\omega_o\omega_c\right) \\ \quad + RCb_0(4\omega_o\omega+2\omega_c\omega+8\omega_o\omega_c\omega) \\ a_3 = 8\omega_o^3\omega_c+\omega_o^4+6\omega_o^2\omega_c^2+LCb_0 \\ \quad \times\left(4\omega_o^3\omega+4\omega_o\omega_c^2\omega+12\omega_o^2\omega_c\omega\right) \\ \quad + RCb_0\left(4\omega_o^3+4\omega_o\omega_c^2+12\omega_o^2\omega_c\right) \\ \quad + RCb_0\left(6\omega_o^2\omega+\omega_c^2\omega+\omega_o\omega_c\omega\right) \\ a_2 = 12\omega_o^4\omega_c+\omega_o^4\omega+4\omega_o^3\omega_c^2+8\omega_o^3\omega_c\omega \\ \quad +6\omega_o^2\omega_c^2\omega+RCb_0\left(4\omega_o^3\omega+12\omega_o^2\omega_c\omega+4\omega_o\omega_c^2\omega\right) \\ a_1 = \omega_o^4\omega_c^2+12\omega_o^4\omega_c\omega+4\omega_o^3\omega_c^2\omega \\ a_0 = \omega_o^4\omega_c^2\omega \end{cases}$$

Because the values of ω_o, ω_c and ω are all positive, so:

$$a_i > 0, \quad (i = 0, 1, 2, 3, 4, 5, 6, 7) \tag{32}$$

The stability of the system is judged by the stability criterion of Leonard chipart algebra, that is, if the odd order herwitz determinant is positive, the system is stable. According to equation (31), $\Delta_3 > 0$, $\Delta_5 > 0$, $\Delta_7 > 0$.

In conclusion, the improved LADRC has good stability.

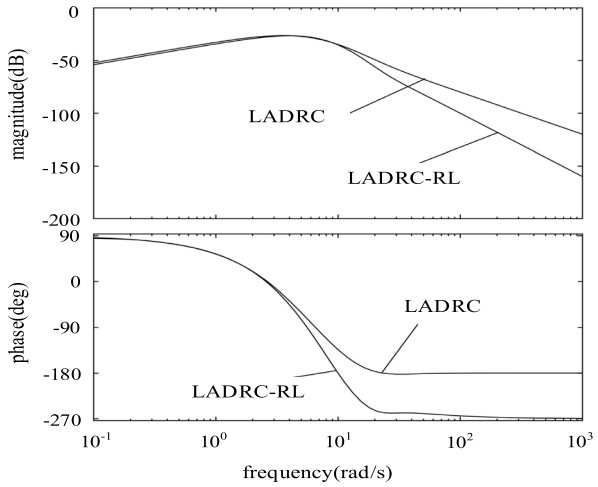

FIGURE 17. Amplitude and phase curves of LADRC-RL and traditional LADRC.

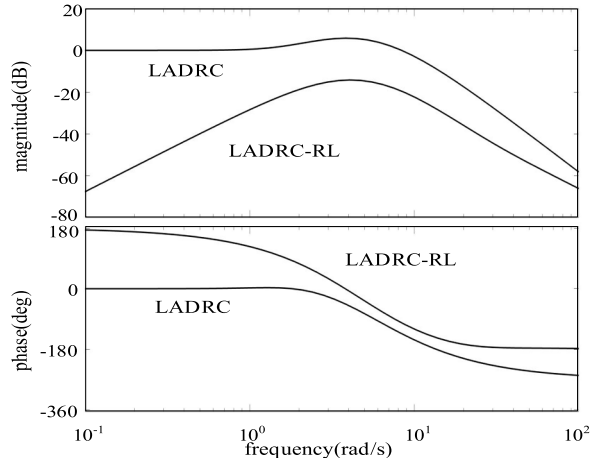

FIGURE 18. Noise amplitude and phase curves of LADRC-RL and traditional LADRC.

D. COMPARATIVE ANALYSIS OF IMPROVED LADRC AND TRADITIONAL LADRC

Figure 17 shows a comparison of LADRC-RL and a conventional LADRC disturbance transfer function, where it can be seen that the high-frequency band gain of LADRC-RL is reduced, and the immunity is enhanced. Simultaneously, there is a phase lag in the system.

Figure 18 shows the LADRC-RL contrast to the traditional LADRC noise transfer function, it can be seen that the noise suppression capability of LADRC-RL is significantly enhanced, and the tracking capability of noise is also superior to that of traditional LADRC.

IV. SIMULATION ANALYSIS

To verify the effectiveness of the LADRC-RL controller with correction link analyzed in this study, a three-phase photovoltaic grid-connected system model was built based on MATLAB simulation software.

TABLE 1. System parameters.

System parameters and units	Numerical value
Grid line voltage /V	380
bus voltage /V	500
Filter resistance /mΩ	1.885
Filter inductor/μH	250
capacitance/μF	20000
Rated frequency /Hz	50

TABLE 2. Controller parameters.

Controller parameters	Numerical value
Controller bandwidth/ω_c	440
Observer bandwidth/ω_o	1800
Controller gain /b	2000000

This simulation is mainly aimed at the influence of different working conditions on the voltage fluctuation of DC-side bus. The regulated working conditions include: light intensity, temperature, load, and unload. The control variable method was used to simulate these three working conditions individually. The core of this model is using of double closed-loop control, and the voltage outer loop is improved and optimized. The current inner loop adopts the traditional PI control, namely LADRC-RL control strategy.

The parameters of photovoltaic grid-connected system and inverter are listed in Tables 1 and 2.

A. DC BUS VOLTAGE FLUCTUATION UNDER STEADY STATE

The steady state is the first key problem in the field of control. The simulation time is 2.5s, the light intensity is 1000W/m^2, the temperature is 25°C, and other conditions are the same. The simulation and comparative analysis of LADRC-RL and LADRC control strategies are performed. The network-side voltage waveform is shown in figure 19, and the DC side bus voltage waveform is shown in figure 20.

As shown in figure 20, when the system is in steady state, the voltage fluctuation range of traditional LADRC is 497.9-502V, and the voltage fluctuation range of LADRC-RL is 498.6-501.4V. When LADRC-RL is in steady state, the peak value of DC bus voltage is 0.6V smaller than LADRC, and the valley value is 0.7V larger than LADRC. The fluctuation range is smaller, and the performance is improved by approximately 0.13%. Therefore, it is concluded that the performance of the LADRC-RL control is better and more effective in a steady state.

B. INFLUENCE OF ILLUMINATION CHANGE ON DC BUS VOLTAGE

The output of the photovoltaic cells is closely related to illumination. Figure 21 shows a schematic diagram of the illumination intensity mutation, which shows a step signal

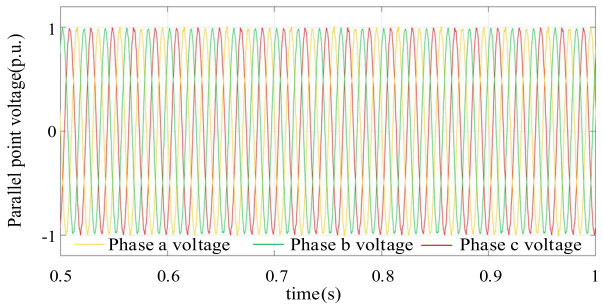

FIGURE 19. Voltage of grid connected PV system under steady state.

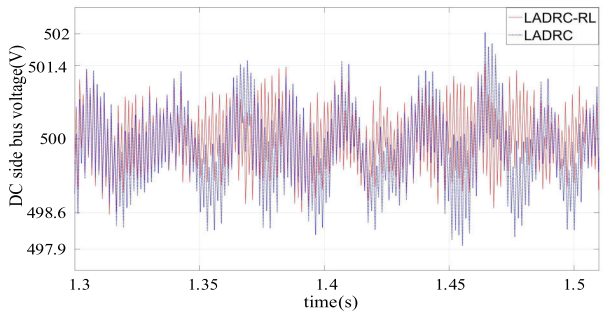

FIGURE 20. Steady state DC bus voltage of photovoltaic grid connected power generation system.

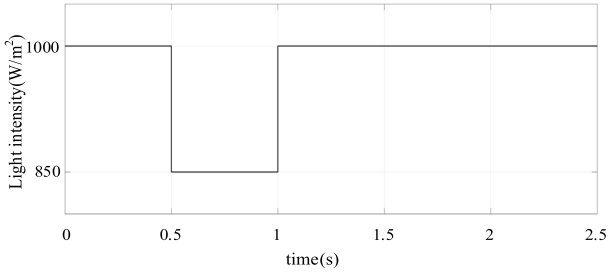

FIGURE 21. Variation of light intensity.

similar to the mutation. The standard illumination intensity is 1000W/m^2 in 0-0.5s. At 0.5 s, the mutation is 850 W/m^2, which is used to simulate the shielding of the panel. At 1s, the mutation is 1000 W/m^2, which is used to simulate the sudden removal of the shielding. The control effect of LADRC-RL and LADRC on the solar PV panel is shown in figure 22.

As can be seen from figure (a), when the solar panel is suddenly blocked, the bus voltage exhibits a downward trend, and after a period of oscillation, it returns to the stability value. From the time domain index analysis, the curve transition time corresponding to LADRC is 0.07s, the valley value is 477.4V, and the overshoot is 4.52%; The curve transition time of LADRC-RL is 0.05s, the valley value is 485V, and the overshoot is 3%.

It can be seen from figure (b) that when the shelter is suddenly removed, the bus voltage first rises, then enters the oscillation link, and finally returns to the steady-state value. The curve transition time of LADRC is 0.08s, the peak value is 523.2V, and the overshoot is 4.63%; The transition time of

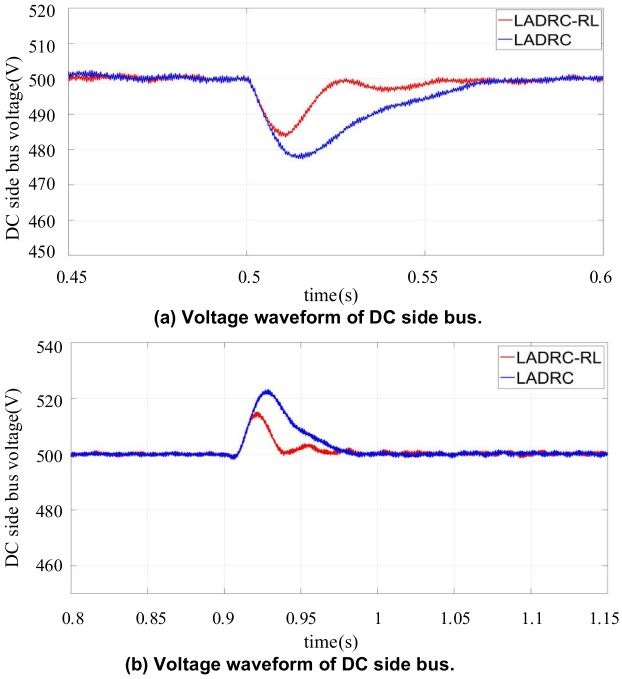

(a) Voltage waveform of DC side bus.

(b) Voltage waveform of DC side bus.

FIGURE 22. Dynamic characteristics of DC bus voltage under light intensity change.

LADRC-RL curve is 0.06s, the peak value is 515V, and the overshoot is 3%.

It can be concluded from the simulation diagram that both of them have no static error in the steady state, but LADRC-RL has a shorter transition time, smaller overshoot, better stability than LADRC under the influence of light, and better anti-interference performance to external environment changes.

C. INFLUENCE OF TEMPERATURE CHANGE ON DC BUS VOLTAGE

The output and temperature of the photovoltaic cell have a certain relationship, and the temperature cannot be mutated, and figure 23 is a simulation of the operating temperature change of the panel. The temperature in 0-1.5s is the working temperature of 25°C under the standard condition, and then after a monotonic increase of 0.05s, it reaches a stable value of 35°C in 1.55s. The control effects of LADRC-RL and LADRC are shown in figure. 24.

As shown in figure 24 when the temperature of the battery board rises sharply, the bus voltage first exhibits a downward trend, and then returns to a steady value after a period of oscillation. From the time domain analysis, the curve transition time corresponding to LADRC is 0.08s, the valley value is 487.4V, and the overshoot is 2.51%; The curve transition time of LADRC-RL is 0.05s, the valley value is 492.7V, and the overshoot is 1.45%.

From the simulation, it can be concluded that the two curves do not have a static error in steady state, but the transition time during the LADRC-RL transition is shorter, and the overshoot is smaller.

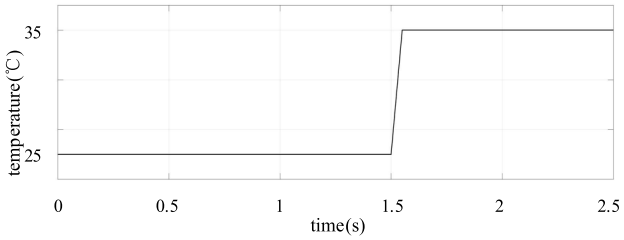

FIGURE 23. Temperature change diagram.

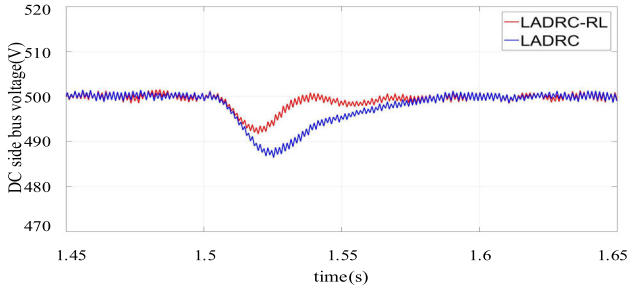

FIGURE 24. Dynamic characteristics of DC bus voltage under temperature change.

D. INFLUENCE OF LOAD VARIATION ON DC BUS VOLTAGE

The grid-side module in the photovoltaic grid-connected power generation system was used to simulate the large power grid system. The grid side parallels the load of 25MW in 2s, and reduces the load of 25MW in 2.3s. The control effects of LADRC-RL and LADRC are shown in figure 25.

As shown in figure 25 (a), the grid voltage decreases significantly during loading and increases again during load shedding. From the qualitative analysis, the load is on the grid, according to the following formula:

$$\Delta U + \delta U = \frac{PR + QX}{U} + \mathrm{j}\frac{PX - QR}{U} \tag{33}$$

The left side of formula (33) is the line voltage drop, P is the active load, Q is the reactive load, U is the load terminal voltage, R and X are the line resistance and reactance respectively, and $R \ll X$ then when the load increases, the line voltage drop increases and the grid voltage decreases. When the load is reduced, the voltage of the power grid increases.

As shown in figure 25 (b), when the load is 25MW in 2s, the DC bus voltage increases a rapidly, reaches its peak value, and then decreases to the steady value; When the load is reduced by 25MW in 2.3s, the DC bus voltage drops rapidly, and then rises to the steady-state value of 500V after reaching the valley value.

Figure 25 (c) shows a partially enlarged diagram of the system loading. The curve transition time corresponding to LADRC is 0.05s, the peak value is 522.8V, and the overshoot is 4.55%; The curve transition time of LADRC-RL is 0.04s, the peak value is 518.1V, and the overshoot is 3.62%.

From the simulation diagram, it can be concluded that LADRC-RL has a shorter transition time and smaller overshoot during loading and unloading.

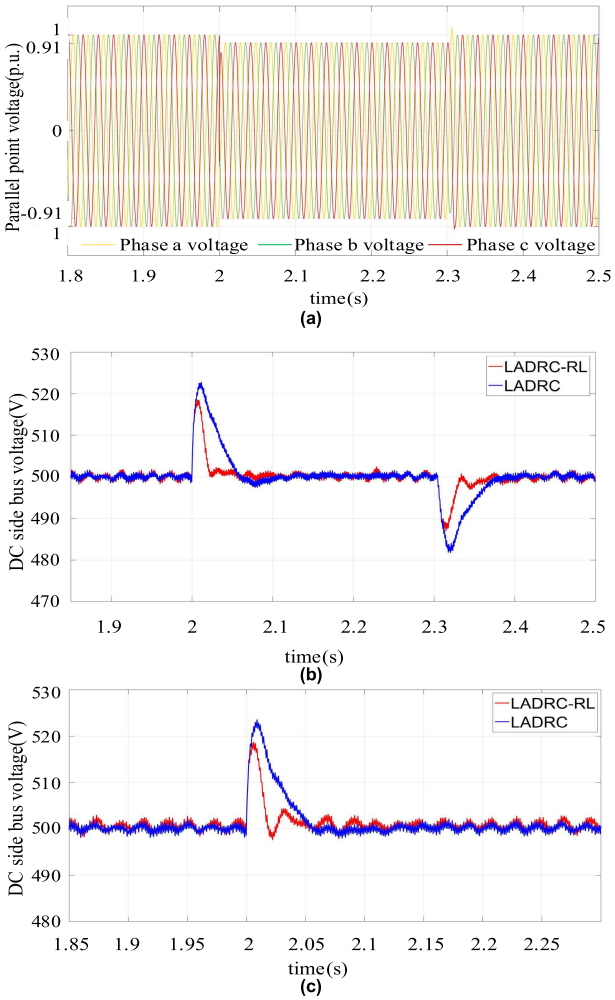

FIGURE 25. Dynamic characteristics of system voltage under load change: (a) Parallel point voltage; (b) Overall dynamic characteristics of loading and unloading; (c) Load simulation.

E. NOISE SUPPRESSION CAPABILITY

To compare the performance of traditional LADRC and LADRC-RL, the same white noise is added to the DC bus voltage. Figure 26 (a) shows the comparison of simulation waveforms of DC bus voltage under traditional LADRC and LADRC-RL control under noise interference. Figure 26 (b) and figure 26 (c) show the grid voltage waveforms under the control of traditional LADRC and LADRC-RL in the presence of noise pollution. Figure 26 (d) and figure 26 (e) show the voltage spectra of traditional LADRC and LADRC-RL controlled parallel nodes under noise pollution.

As can be seen from figure 26 (a), the fluctuation range of DC us voltage controlled by traditional LADRC in steady state is 488.8-512.6V, and the fluctuation range of LADRC-RL is 494.9-506.1V. Therefore, the traditional LADRC will make the DC bus voltage oscillate greatly, and LADRC-RL can obviously suppress the influence of noise on the system. As can be seen from figure 26 (b) and figure 26 (c), when the traditional LADRC controlled grid-connected inverter is affected by noise, the grid-connected voltage waveform

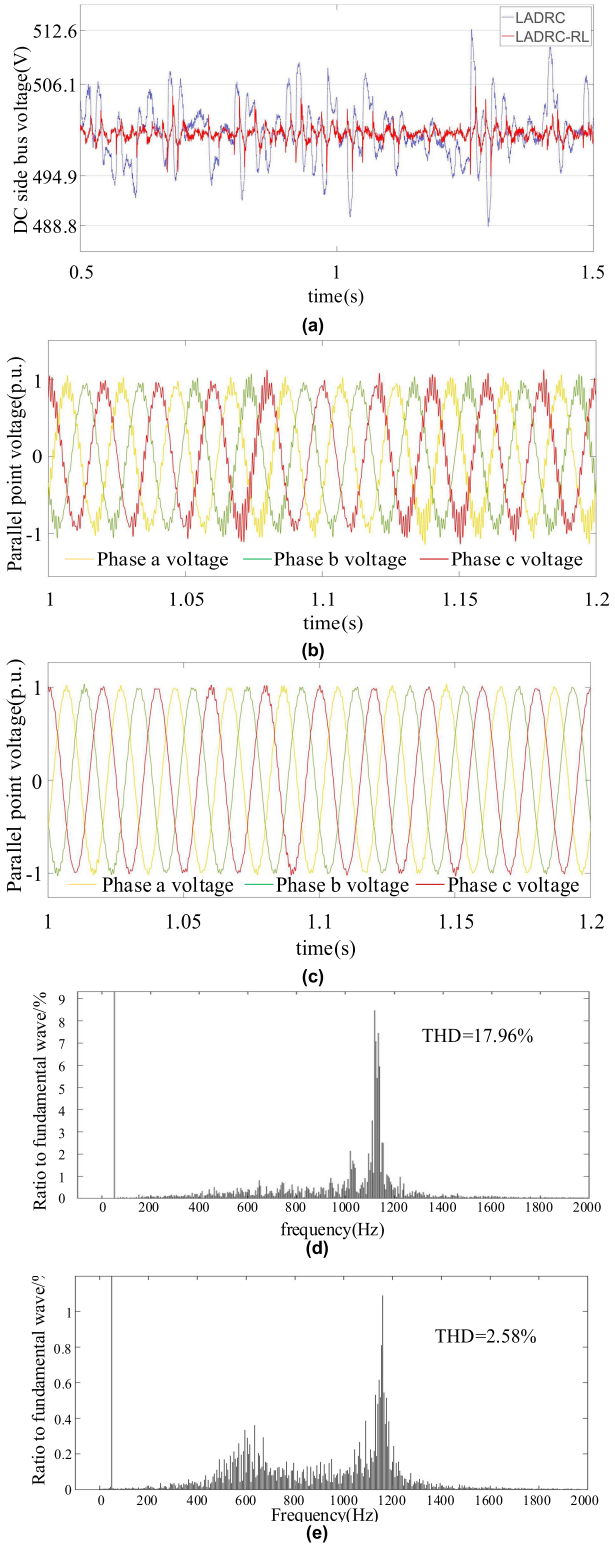

FIGURE 26. Dynamic characteristics of system voltage with white noise added: (a) DC bus voltage waveform; (b) Grid connected voltage waveform controlled by traditional LADRC; (c) Grid connected voltage waveform controlled by LADRC-RL; (d) Voltage spectrums of traditional LADRC control; (e) Voltage spectrums of LADRC-RL control.

will be seriously distorted, whereas when the LADRC-RL controlled grid-connected inverter is affected by noise, the sinusoidal degree of grid-connected voltage waveform is greatly improved, close to the sine wave. As can be seen from figure 26 (d) and figure 26 (e), when LADRC-RL control is adopted, the harmonic distortion rate of grid-connected voltage is reduced from 17.96% to 2.58%, meeting the national standard of harmonic requirements. The simulation results show that LADRC-RL control can significantly improve the performance of a system with noise pollution.

V. CONCLUSION

To improve the performance of traditional LADRC control strategies, this chapter adds a first-order inertial link based on traditional LESO, and solves the problem of high-frequency noise. In this study, the voltage outer ring is improved in the dual closed loop control in the double closed-loop control. Through frequency domain analysis, the improved control effect increases high-frequency attenuation capability and anti-interference ability. LADRC-RL control is more effective than traditional LADRC control strategies.

By changing the conditions such as lighting intensity, temperature and load, this study analyzes the control performance of traditional LADRC and LADRC-RL. The simulation results show that the LADRC-RL-based voltage outer ring controller has good dynamic performance, which can quickly achieve steady state, strong anti-interference ability, and can better stabilize the system, DC bus voltage and anti-interference performance both of which are superior to traditional LADRC. This new double closed-loop structure can better stabilize the DC bus voltage, improve system reliability and economy, and provide a good reference value for safe operation of the photovoltaic power generation.

The next research direction is to use the intelligent algorithm to optimize parameter adjustment, so that the controller achieves a more ideal level in practice.

REFERENCES

[1] N. Priyadarshi, V. Ramachandaramurthy, S. Padmanaban, and F. Azam, "An ant colony optimized MPPT for standalone hybrid PV-wind power system with single Cuk converter," *Energies*, vol. 12, no. 1, p. 167, Jan. 2019.

[2] P. Madasamy, R. Verma, A. Rameshbabu, A. Murugesan, R. Umamageswari, J. L. Munda, C. Bharatiraja, and L. Mihet-Popa, "Neutral point clamped transformer-less multilevel converter for grid-connected photovoltaic system," *Electronics*, vol. 10, no. 8, p. 977, Apr. 2021.

[3] Z.-X. Liao, D. Luo, X.-S. Luo, H.-S. Li, Q.-Q. Xiang, G.-X. Huang, T.-H. Li, and P.-Q. Jiang, "Nonlinear model and dynamic behavior of photovoltaic grid-connected inverter," *Appl. Sci.*, vol. 10, no. 6, p. 2120, Mar. 2020.

[4] X. Zhou, Q. Liu, Y. Ma, and B. Xie, "DC-link voltage research of photovoltaic grid-connected inverter using improved active disturbance rejection control," *IEEE Access*, vol. 9, pp. 9884–9894, 2021.

[5] L. Hassaine and M. R. Bengourina, "Control technique for single phase inverter photovoltaic system connected to the grid," *Energy Rep.*, vol. 6, pp. 200–208, Feb. 2020.

[6] M. Y. Ali Khan, H. Liu, Z. Yang, and X. Yuan, "A comprehensive review on grid connected photovoltaic inverters, their modulation techniques, and control strategies," *Energies*, vol. 13, no. 16, p. 4185, Aug. 2020.

[7] M. Shadoul, H. Yousef, R. Al Abri, and A. Al-Hinai, "Adaptive fuzzy approximation control of PV grid-connected inverters," *Energies*, vol. 14, no. 4, p. 942, Feb. 2021.

[8] L. Song, L. Huang, B. Long, and F. Li, "A genetic-algorithm-based DC current minimization scheme for transformless grid-connected photovoltaic inverters," *Energies*, vol. 13, no. 3, p. 746, Feb. 2020.
[9] H. Xiao, "Overview of transformerless photovoltaic grid-connected inverters," *IEEE Trans. Power Electron.*, vol. 36, no. 1, pp. 533–548, Jan. 2021.
[10] Z. Zhang, P. Wang, F. Gao, Z. Liu, J. Zhang, and P. Jiang, "Research on synchronous control method for suppressing nonlinear impulse perturbation of photovoltaic grid-connected inverter," *IEEE Access*, vol. 8, pp. 22303–22313, 2020.
[11] Z. Zhang, Z. Li, M. P. Kazmierkowski, J. Rodriguez, and R. Kennel, "Robust predictive control of three-level NPC back-to-back power converter PMSG wind turbine systems with revised predictions," *IEEE Trans. Power Electron.*, vol. 33, no. 11, pp. 9588–9598, Nov. 2018.
[12] P. Magne, D. Marx, B. Nahid-Mobarakeh, and S. Pierfederici, "Large-signal stabilization of a DC-link supplying a constant power load using a virtual capacitor: Impact on the domain of attraction," *IEEE Trans. Ind. Appl.*, vol. 48, no. 3, pp. 878–887, May 2012.
[13] M. M. N. Amin and O. A. Mohammed, "DC-bus voltage control technique for parallel-integrated permanent magnet wind generation systems," *IEEE Trans. Energy Convers.*, vol. 26, no. 4, pp. 1140–1150, Dec. 2011.
[14] B.-G. Gu and K. Nam, "A DC-link capacitor minimization method through direct capacitor current control," *IEEE Trans. Ind. Appl.*, vol. 42, no. 2, pp. 573–581, Apr. 2006.
[15] S. A. OLiveira da Silva, L. P. Sampaio, F. Marcos de Oliveira, and F. R. Durand, "Feed-forward DC-bus control loop applied to a single-phase grid-connected PV system operating with PSO-based MPPT technique and active power-line conditioning," *IET Renew. Power Gener.*, vol. 11, no. 1, pp. 183–193, Jan. 2017.
[16] J. Han, "From PID to active disturbance rejection control," *IEEE Trans. Ind. Electron.*, vol. 56, no. 3, pp. 900–906, Mar. 2009.
[17] J. Q. Han, *Active Disturbance Rejection Control Technique the Technique for Estimating and Compensating the Uncertainties*. Beijing, China: National Defense Industry Press, 2008.
[18] B. Long, W. Wang, L. Huang, Y. Chen, F. Li, H. Sun, and H. Li, "Design and implementation of a virtual capacitor based DC current suppression method for grid-connected inverters," *ISA Trans.*, vol. 92, pp. 257–272, Sep. 2019.
[19] Y. Yang, L. Ma, D. Huang, and N. Qin, "Output feedback repetitive learning control of an electrohydraulic actuator of a lower limb rehabilitation exoskeleton," *Comput. Sci. Eng.*, vol. 21, no. 6, pp. 6–19, Nov. 2019.
[20] X. Feng, X. Cui, W. Ma, and S. Wang, "Double closed-loop control strategy of three-phase Vienna rectifier based on unbalanced grid," *Power Syst. Technol.*, vol. 45, no. 5, pp. 1976–1984, 2021.
[21] S. Kan, X. Ruan, X. Huang, and H. Dang, "Second harmonic current reduction for flying capacitor clamped boost three-level converter in photovoltaic grid-connected inverter," *IEEE Trans. Power Electron.*, vol. 36, no. 2, pp. 1669–1679, Feb. 2021.
[22] Z. Gao, "Active disturbance rejection control: A paradigm shift in feedback control system design," in *Proc. Amer. Control Conf.*, Minneapolis, MN, USA, Jun. 2006, p. 7.
[23] A. Benrabah and D. Xu, "UDE-based current control of grid-connected photovoltaic inverters," *Int. J. Comput. Math. Electr. Electron. Eng.*, vol. 38, no. 1, pp. 183–198, Jan. 2019.
[24] M. Elkayam and A. Kuperman, "Optimized design of multiresonant AC current regulators for single-phase grid-connected photovoltaic inverters," *IEEE J. Photovolt.*, vol. 9, no. 6, pp. 1815–1818, Nov. 2019.
[25] M. B. Satti and A. Hasan, "Direct model predictive control of novel H-bridge multilevel inverter based grid-connected photovoltaic system," *IEEE Access*, vol. 7, pp. 62750–62758, 2019.
[26] D. Wu and K. Chen, "Frequency-domain analysis of nonlinear active disturbance rejection control via the describing function method," *IEEE Trans. Ind. Electron.*, vol. 60, no. 9, pp. 3906–3914, Sep. 2013.
[27] C. Jia, L. Wang, E. Meng, L. Chen, Y. Liu, W. Jia, Y. Bao, and Z. Liu, "Combining LIDAR and LADRC for intelligent pitch control of wind turbines," *Renew. Energy*, vol. 169, pp. 1091–1105, May 2021.
[28] H. R. Daiha and G. S. Deaecto, "$\mathcal{H}_2$ static output feedback switching function design based on a time-varying Lyapunov function approach," *Int. J. Control*, vol. 94, no. 6, pp. 1484–1491, Jun. 2021.
[29] S. W. Li, Y. L. Sun, J. G. Jin, and Q. Li, "Power quality control method of micro grid based on control strategy of inverter distributed power supply," *Grid Technol.*, vol. 34, pp. 6–11, Oct. 2010.
[30] Z. Pan, X. Wang, T. T. G. Hoang, Z. Wang, and L. Tian, "DC-link voltage disturbance rejection strategy of PWM rectifiers based on reduced-order LESO," *IEEE Access*, vol. 7, pp. 103693–103705, 2019.
[31] X. Xu, X. Zhou, Y. Ma, and Z. Gao, "Micro grid operation controller based on ADRC," *High Volt. Eng.*, vol. 42, pp. 3336–3346, Mar. 2016.

BO ZHANG received the M.S. degree from the School of Electrical Engineering, Tianjin University of Technology, China, in 2021. His research interests include active disturbance rejection control technology and grid inverter.

XUESONG ZHOU received the B.S. degree from South China University of Technology, Guangzhou, China, in 1984, and the M.S. and Ph.D. degrees from Tsinghua University, Beijing, China, in 1990 and 1993, respectively. From 1993 to 2002, he worked with the School of Electrical and Automation Engineering, Qingdao University, as the Deputy Dean and the Director of Shandong Provincial Key Laboratory of Power Electronics Engineering. In 1997, he was promoted to a Full Professor at Qingdao University. Since 2002, he has been working with the School of Electrical and Electronic Engineering, Tianjin University of Technology, Tianjin, China. His research interests include power system analysis and automation, smart grid, and the field of new energy utilization.

YOUJIE MA received the B.S., M.S., and Ph.D. degrees from Tsinghua University, Beijing, China, in 1987, 1990, and 1993, respectively. From 1993 to 2002, she worked with the School of Electrical and Automation Engineering, Qingdao University, where she was promoted to a Full Professor, in 1998. Since 2002, she has been working as a Distinguished Professor with the School of Electrical and Electronic Engineering, Tianjin University of Technology, Tianjin, China. Her research interests include power system analysis and automation and smart grid.